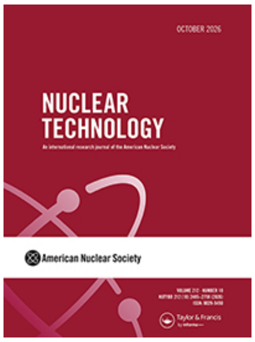

Nuclear Technology

ISSN: 0029-5450 (Print) 1943-7471 (Online) Journal homepage: www.tandfonline.com/journals/unct20

Effect of Crack Location on the Mechanical State at the Tip of Stress Corrosion Cracks in Dissimilar Metal Welded Joints

Shuai Wang , Yicheng Wang , Bin Wang , Wanzhong Li , Lu Cui , Shaohu Liu , Lijing Dong & He Xue

To cite this article: Shuai Wang , Yicheng Wang , Bin Wang , Wanzhong Li , Lu Cui , Shaohu Liu , Lijing Dong & He Xue (17 Aug 2026): Effect of Crack Location on the Mechanical State at the Tip of Stress Corrosion Cracks in Dissimilar Metal Welded Joints, Nuclear Technology, DOI: 10.1080/00295450.2026.2707617

To link to this article: https://doi.org/10.1080/00295450.2026.2707617

Published online: 17 Aug 2026.

NUCLEAR TECHNOLOGY

DOI: https://doi.org/10.1080/00295450.2026.2707617

Effect of Crack Location on the Mechanical State at the Tip of Stress Corrosion Cracks in Dissimilar Metal Welded Joints

Shuai Wang[a,b], Yicheng Wang[a], Bin Wang[b], Wanzhong Li[a], Lu Cui[a], Shaohu Liu[a], Lijing Dong[c], and He Xue[d]

[a]*School of Mechanical Engineering, Xi'an Petroleum University, Xi'an, China;* [b]*Department of Mechanical and Aerospace Engineering, Brunel University of London, Uxbridge, United Kingdom;* [c]*School of New Energy and Materials, Southwest Petroleum University, Chengdu, China;* [d]*School of Mechanical Engineering, Xi'an University of Science and Technology, Xi'an, China*

Received April 7, 2026
Accepted for Publication July 15, 2026

Abstract — *Dissimilar metal weld joints (DMWJs) between low-alloy steel SA508 and austenitic stainless steel 316L, fabricated using nickel-based alloy 52M as filler metal, are critically important in the primary circuit of pressurized water reactors (PWRs). The structural integrity of such DMWJs is strongly influenced by the mechanical heterogeneity, especially near the fusion line (FL). In this study, the local mechanical properties of an SA508-52M-316L DMWJ were determined via an indentation test, while metallographic analysis was employed to characterize the heterogeneous microstructure adjacent to the FL. A finite element (FE) model incorporating continuously graded mechanical properties was developed using a predefined temperature field approach to represent the material heterogeneity more accurately than conventional sandwich models. Based on this continuous transition model, elastoplastic FE analyses were conducted to evaluate the Mises stress and plastic strain distributions at the tip of cracks located at different positions relative to the FL. The results reveal that the inhomogeneous mechanical property distribution significantly alters the crack-driving force, particularly when the crack approaches the FL region, underscoring the necessity of accounting for local heterogeneity in the structural integrity assessment of DMWJs.*

Keywords — *Welded joints, stress corrosion cracks, mechanical state of crack tip, mechanical heterogeneity.*

I. INTRODUCTION

The dissimilar metal weld joint (DMWJ) between low-alloy steel SA508 and 316L austenitic stainless steel (SS) piping is a critical component extensively utilized in the primary coolant circuits of pressurized water reactors (PWRs) within nuclear power plants. Such joints, typically incorporating a nickel-based filler metal such as alloy 52M to mitigate issues such as carbon migration, are primarily employed in nozzle-to-safe-end connections for reactor pressure vessels, ensuring the structural integrity of the core containment system under demanding operational conditions [1,2].

The low-alloy steel SA508 is typically employed in the fabrication of pressure vessels and pipe nozzles in nuclear power plants (NPPs), owing to its favorable combination of strength, favorable ductility, cost-effectiveness, and commendable resistance to neutron irradiation embrittlement [3,4]. To enhance corrosion resistance in the high-temperature, high-pressure aqueous environment of the primary circuit, a 316L austenitic stainless piping is applied. This configuration results in a DMWJ that integrates three distinct metallic materials, each with unique mechanical and physicochemical properties. The primary engineering objective of this heterogeneous material system is to synergistically leverage the

CONTACT Bin Wang bin.wang@brunel.ac.uk

advantageous characteristics of each constituent. However, this joint has been observed to exhibit susceptibility to stress corrosion cracking (SCC) within primary water environments, presenting considerable concerns for the structural integrity and operational safety of PWRs [5,6]. Such cracking degradation predominantly initiates and propagates along the fusion line (FL) and the heat-affected zone (HAZ) of the weldment [7,8].

Given the difficulties in performing maintenance or replacement on irradiated components in the primary circuit of NPPs over their full life cycle, extensive studies have been devoted to the mechanical properties of DMWJs in their initial state. For microstructural and mechanical characterization, Sun et al. [9] investigated the stress corrosion crack growth rate (SCCGR) of a 20% cold-worked 316LN SS/Inconel 52M fusion boundary (FB) (20%CW 316LN/52M-FB) in simulated PWR primary water. Their results indicated that the SCCGR at the 20%CW 316LN/52M-FB was five to six times higher than that of a non-cold-worked 316L/52M-FB [9]. Okonkwo et al. [10,11] employed electron backscattered diffraction (EBSD) to analyze the grain size across the refined, partially refined, and base metal (BM) matrix regions within the HAZ of an SA508-309L/308L DMWJ. The yield strength of the HAZ was subsequently determined using the Hall–Petch correlation derived from the grain size data. Nevertheless, the predictive capability of this EBSD-based approach calls for further experimental verification to confirm its reliability across different DMWJ conditions [10,11].

On the fracture behavior of DMWJs, Wang et al. [12] developed a coupled numerical approach integrating the extended finite element method (XFEM) and a De-bond submodel to investigate crack growth behavior in DMWJs. Their simulations, which accounted for continuous transitions in local mechanical properties, revealed that crack paths are significantly influenced by mechanical heterogeneity, with SCC demonstrating a propensity to propagate toward regions of higher yield strength due to a greater crack driving force in these areas [12]. Zhao et al. [13] introduced a constraint parameter, D_p, incorporating both in-plane and out-of-plane constraints, which is defined by the equivalent plastic strain (PEEQ) gradient near the crack front in DMWJs. Utilizing the User-Defined Field (USDFLD) subroutine, they achieved a continuous transition of mechanical properties aligned with the joint's geometry, while the submodel technique enabled a detailed analysis of the crack-tip constraint under complex loading conditions. Their findings indicate that cracks located at the specimen center possess a higher propensity for propagation compared to surface cracks, with the SA508/52Mb interface identified as the most critical location within the DMWJs [13]. Yang and Wang [14] systematically investigated the fracture behavior of nuclear safety-end DMWJs under different constraints, considering the effect of residual stresses introduced via a restart method after applying localized pre-loads to single-edge notched bend (SENB) specimens. Their results demonstrated that residual stresses significantly influence the fracture behavior, with the J-R curve of high-constraint specimens being more sensitive to residual stress variations compared to low-constraint specimens [14]. Based on the Vickers hardness test and stress-hardness correlation, Wang et al. [15] characterized the heterogeneous mechanical properties of the DMWJ with continuous transition. The results show that the gradient in mechanical properties considerably enhances the crack driving force near the FL, underscoring the need to account for local property variations in the integrity assessment of DMWJs [15]. Zhang et al. [16] systematically examined the influence of strength mismatch and work hardening mismatch on the stress and strain fields at SCC crack tips in dissimilar metal welded joints using a finite element (FE) method under small-scale yielding conditions. Their findings demonstrate a pronounced influence of these mismatch parameters on the plastic zone and stress state within the weld metal (WM), contrasted by a negligible effect in the BM, while the J-integral decreased with an individual increase in either mismatch type [16]. Gu et al. [17] investigated the fracture behavior of nuclear safety-end DMWJs by introducing localized residual stresses into SENB specimens via a pre-loading and restart method. Their results demonstrated that residual stresses, whether tensile or compressive depending on the pre-load location, respectively decreased or increased the J-R curve, with high-constraint specimens exhibiting greater sensitivity to these stresses compared to low-constraint specimens [17]. Overall, existing scholarly efforts in analyzing SCC growth behavior in DMWJs have not yet comprehensively integrated the variations in mechanical properties induced by the welding process into the calculation of crack-tip mechanical fields. This omission may lead to insufficient accuracy in predicting the crack propagation behavior.

This investigation accounted for the heterogeneous distribution of mechanical properties within the DMWJ; the mechanical properties along the direction transverse to the fusion line were determined via indentation testing. Subsequently, an elastoplastic FE model incorporating continuously graded mechanical properties (i.e., continuous model) across the FL was developed. Numerical simulations were subsequently performed to quantify discrepancies in the crack-tip mechanical states predicted by this continuous model versus a conventional sandwich model. The findings contribute to enhanced precision in structural integrity assessments for DMWJs.

II. EXPERIMENTS

II.A. Materials and Specimen

The DMWJ with a material configuration of SA508-52M-316L was adopted for investigation. Fig. 1a illustrates a full-scale model of the DMWJ, and the joint integrates 316L SS at the piping terminus, valued for its superior corrosion resistance, with SA508 alloy steel serving as the base material at the reactors pressure vessel. A nickel-base alloy, alloy 52M, is utilized as the WM; within the DMWJ, the specific variant applied on the pressure vessel side (SA508 side) is denoted as 52Mb, while that on the piping side (316L side) is designated as 52Mw. The cladding is fabricated by depositing 308/309L SS using shielded metal arc welding, which serves as a corrosion-resistant cladding on the SA508 pressure vessel side [15].

This structural configuration is designed to leverage the respective advantages of the constituent materials, thereby potentially enhancing the service longevity of the DMWJ. The specimen (SA508-52M-316L) utilized for indentation testing in this study was extracted from an actual DMWJ. The location from which the specimen was cut, indicated by a red dashed rectangle, and the specimen itself are presented in Fig. 1 [18,19].

II.B. Indentation Test

Given the inherent mechanical heterogeneity characteristic of DMWJs, conventional uniaxial tensile testing is inadequate for characterizing the mechanical properties across the joint region. To address this limitation, a customized indentation testing apparatus was utilized to inversely determine the distribution of mechanical properties within the welded joint. Owing to its minimal thickness (7 mm), the 309L/308L SS cladding was disregarded in the indentation test. The quasi-static indentation behavior was evaluated using a UTM-6103 universal testing machine equipped with a tungsten carbide spherical indenter (radius = 0.5 mm) to ensure high rigidity. Tests were conducted under displacement control at a constant rate of 0.1 mm/min until a penetration depth of 0.1 mm was achieved. Furthermore, to guarantee experimental consistency, the ambient temperature was strictly regulated, with fluctuations maintained below 0.2°C/h. The indentation experiments were conducted in compliance with the specifications outlined in the standard GB/T 22 458–2008, with a spacing of 2 mm maintained between adjacent indentation locations [20]. To increase

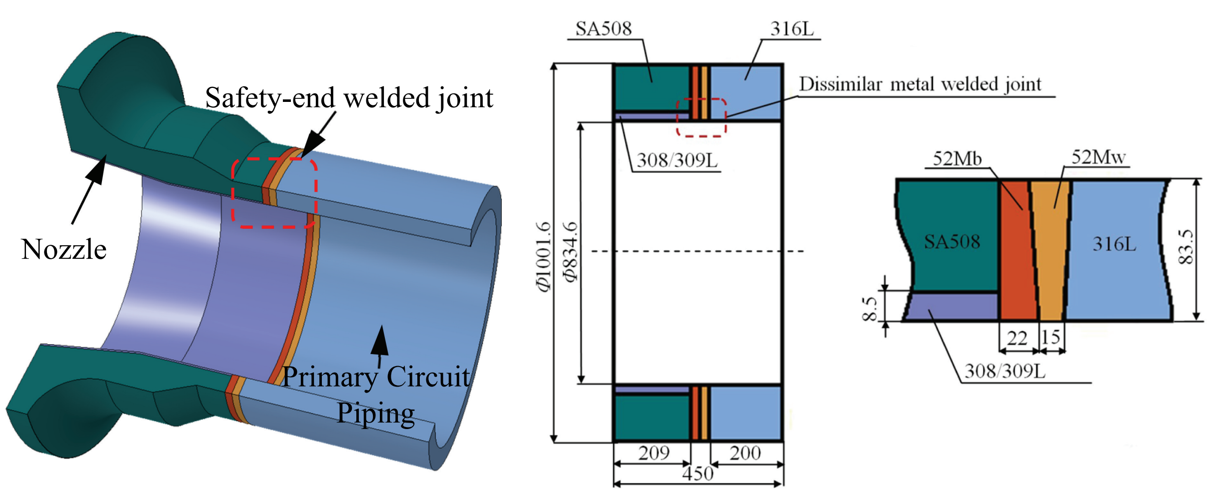

(a) The structure and composition of DMWJ for nuclear power safety ends.

(b) The dimensional parameters of DMWJ

Fig. 1. A typical DMWJ in nuclear Reactor Pressure Vessel (RPV) /safe-end connections.

the spatial density of measurements, a staggered distribution pattern comprising two sets of test points was implemented, with an inter-set separation of 5 mm. The final indentation layout applied to the welded specimen, comprising a total of 49 measurement points, is depicted in Fig. 2. For comprehensive details regarding the methodology for extracting mechanical properties of DMWJs via indentation testing, readers are referred to Ref. [21]. Central to this analysis is the derivation of constitutive properties from indentation data. Utilizing the Hollomon hardening law, an FE model was constructed to define the mapping function between the indentation signatures (the maximum load F_{max}, residual depth h_r) and the elastoplastic parameters (yield strength σ_y, strain-hardening exponent n). The experimental indentation data, acquired perpendicular to the welding direction, were subsequently processed through this inversion algorithm to quantify the local mechanical properties of the joint. It should be noted that Figs. 2 and 3 are presented as schematics to clearly delineate the measurement point locations, rather than to-scale engineering drawings of the test specimens.

II.C. Microstructure Analysis

Microstructural analysis was performed on a DMWJ specimen from the safe-end region, using a Leica DM2700M metallographic microscope. The specific sampling locations for microstructural analysis are shown in Fig. 3.

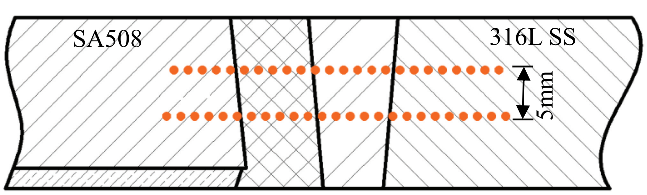

Fig. 2. Indentation test area [21].

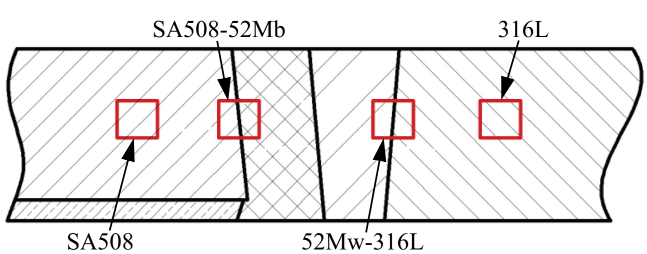

Fig. 3. Microstructure scanning area.

Specimens from these locations were sectioned via wire cutting and ground sequentially up to 2000-grit silicon carbide paper using a YMPZ-1 automatic metallographic grinding and polishing machine. The surfaces to be examined were then polished to a final finish of 2.5 μm. Appropriate etchants were selected for the different materials involved; the etched surfaces were subsequently observed for metallographic characterization. The specific etchants used are summarized in Table 1.

III. FINITE ELEMENT MODEL ANALYSIS

III.A. Constitutive Model

Owing to the geometrical constraints of the HAZ, extracting standard tensile specimens from the SA508-52M-316L DMWJ is often infeasible. Consequently, indentation testing is widely employed to characterize mechanical properties, especially within localized regions such as the FL, where significant gradients in mechanical behavior are present. This study utilizes a constitutive model, derived from a previously established computational method within our research group, to determine the mechanical property distribution across the DMWJ. The resulting distributions of yield stress and the hardening exponent for the SA508-52M-316L DMWJ are presented in Figs. 4 and 5, respectively [21,22].

The quantitative relationships among yield stress (σ_y), strain hardening exponent (n), and distance (D) across key regions of the welded joint—specifically, the SA508 BM, the 316L HAZ, and the WMs (52Mb and 52Mw)—were derived using the Curve Fitting Toolbox in MATLAB. The fitting equations formulated for the interface between the SA508 HAZ and the 52Mb WM, along with their corresponding goodness-of-fit metrics, are presented below [21,22].

TABLE 1

Types of Etchants Employed for Different Zones of the DMWJ

Location	Etching solution
SA508	4% nital (4 mL nitric acid and 96 mL ethanol)
52Mb	10% chromic acid
52Mw	16 g $FeCl_3$ + 2 mL HNO_3 + 80 mL HCl +11 mL H_2O
316L	

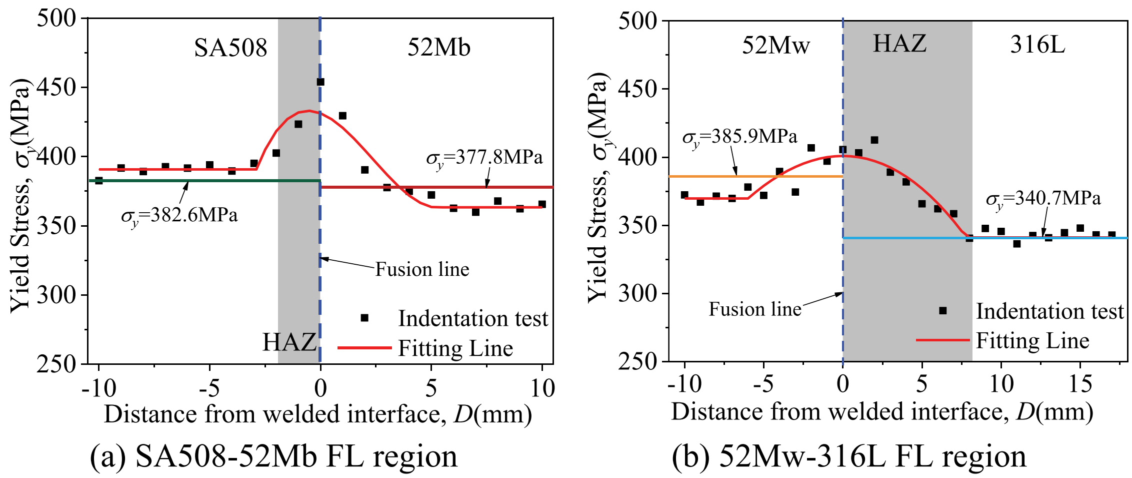

Fig. 4. Yield stress distribution across the SA508-52M-316L DMWJ [21,22].

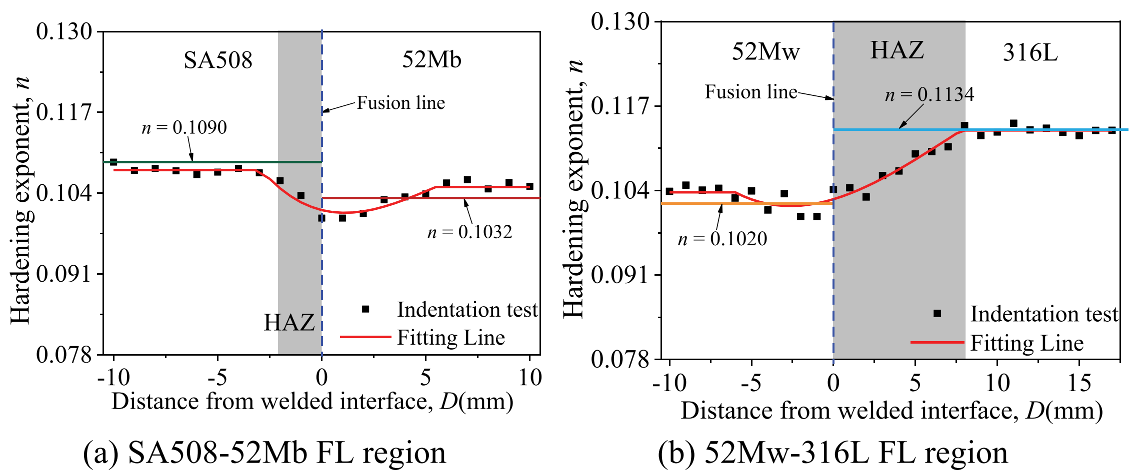

Fig. 5. Hardening exponent distribution across the SA508-52M-316L DMWJ [21,22].

$$\sigma_y = 0.698D^3 - 4.946D^2 - 6.244D + 431.2, R^2 = 0.8223 \tag{1}$$

$$n = -2.539 \times 10^{-5}D^3 + 4.116 \times 10^{-4}D^2 - 8.18 \times 10^{-4}D + 0.101, R^2 = 0.8702 \tag{2}$$

For the interface location between the WM 52Mw and the 316L HAZ:

$$\sigma_y = -8.443 \times 10^{-3}D^3 - 0.3605D^2 + 28.12D + 46.66, R^2 = 0.8262 \tag{3}$$

$$n = -5.669 \times 10^{-6}D^3 - 4.956 \times 10^{-4}D^2 - 0.0128D + 0.205, R^2 = 0.9092 \tag{4}$$

The Young's modulus values of SA508, 52M, and 316L SS were determined as 202.41 GPa, 178.13 GPa, and 196 GPa, respectively, based on Refs. [23–25]. To accurately represent the gradual transition of mechanical properties across the DMWJ, a material model incorporating continuous property variation, referred to as the continuous model was developed using a predefined temperature field approach.

The sandwich model represents an established approach for characterizing the mechanical behavior of welded joints. In this investigation, the DMWJ was delineated into distinct zones within the sandwich model framework, with each constituent material assigned specific yield stress (σ_y) and strain hardening exponent (n) values, for simplification, the mechanical properties of the HAZ were considered identical to those of the BM. To facilitate comparison, the von

TABLE 2

The Mechanical Parameters for the Sandwich Model [22]

Material	Young's modulus, E/MPa	Yield stress, σ_y/MPa	Hardening exponent, n
SA508	202 410	382.6	0.1090
316L	196 000	340.7	0.1134
52Mb	178 130	377.8	0.1032
52Mw	178 130	385.9	0.1020

Mises stress and the plastic strain on the crack tip were computed concurrently for both the sandwich model and the continuous model utilizing the same FE analysis framework. The mechanical parameters adopted for the four materials in the sandwich model are summarized in Table 2 [22]. To delineate the distinction in material parameterization between the sandwich and continuous transition models, in Figs. 4 and 5, respectively, the mechanical properties of SA508, 52Mb, 52Mw, and 316L (as specified in Table 2) are represented by solid lines in dark green, dark red, orange, and light blue, respectively, corresponding exclusively to the sandwich model configuration.

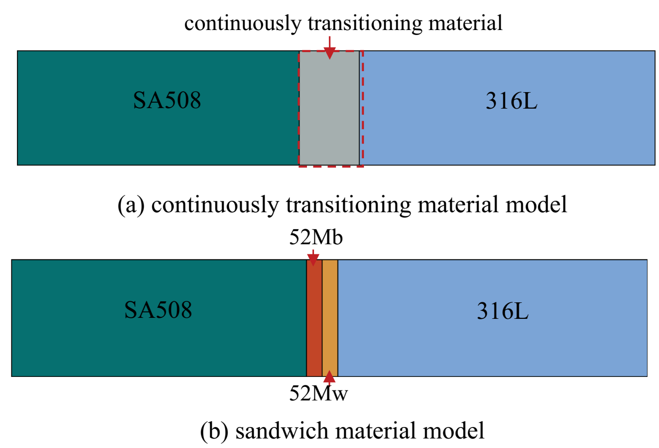

Fig. 6. Comparison between the continuously transitioning material model and the sandwich model.

III.B. Geometric Model

By utilizing temperature-dependent field variables in ABAQUS, the continuously varying temperature field served as an intermediary to assign the gradually transitioning hardening exponent n and yield stress σ_y from Figs. 4 and 5 to the numerical model, thereby achieving continuously graded mechanical properties in the material model, as illustrated in Fig. 6a. Meanwhile, to compare the differences in computational results between the model with continuously graded mechanical properties and the traditional sandwich model, a sandwich material model was also developed, as illustrated in Fig. 6b. It is pertinent to mention that the 309L/308L SS cladding, characterized by a nominal thickness of 7 mm, was rationally omitted from the numerical domain. This decision was predicated on the necessity of geometrical simplification to mitigate computational complexity and facilitate a tractable analysis.

III.C. Finite Element Models

Based on the actual geometry and dimensions of the weld joint provided in Fig. 1, a global model was developed as illustrated in Fig. 7a. Subsequently, a submodel containing a crack, measuring 74 mm × 20 mm, was extracted from the inner wall of the pipe near the weld seam, as depicted in Fig. 7b. To more accurately analyze the influence of crack location within the heterogeneous weld joint on the mechanical fields at the crack tip, including the stress and strain fields, a secondary submodel with a diameter of 0.5 mm was constructed, as shown in Fig. 7c. In Fig. 7, the positive x-axis direction is defined as perpendicular to the weld seam, while the positive y-axis direction is parallel to the weld seam.

To analyze the influence of different crack positions on the crack-tip mechanical fields, an investigation was conducted on cracks originating from specific locations: crack #2 at the SA508–52Mb fusion line within the weld, interface crack #5 at the 52Mw–316L fusion line, and sub-interface cracks situated 1 mm away from the fusion line in the base metals SA508, 316L, and 52M, designated as cracks #1, #3, #4, and #6, respectively. The crack lengths were set uniformly to 6 mm for all cases. The specific distribution of these crack locations is illustrated in Fig. 8.

The global model, primary submodel, and the secondary submodel are illustrated in Figs. 9a, 9b, and Figs. 9d, respectively. All these models were discretized using four-node bilinear axisymmetric elements (CAX4). The global model comprised 5343 elements, the primary submodel

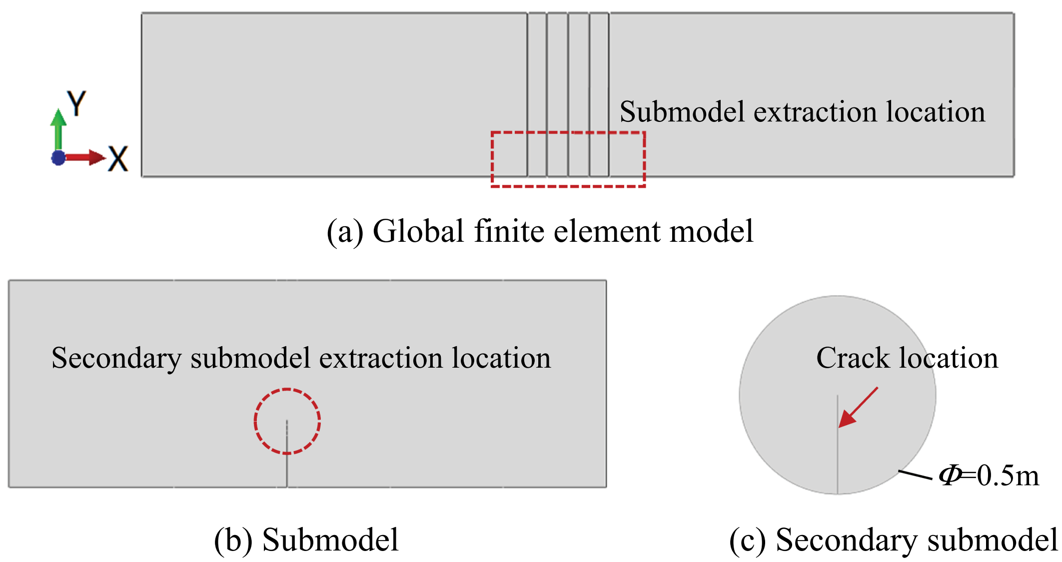

Fig. 7. Geometric model of the welded joint containing SCC cracks.

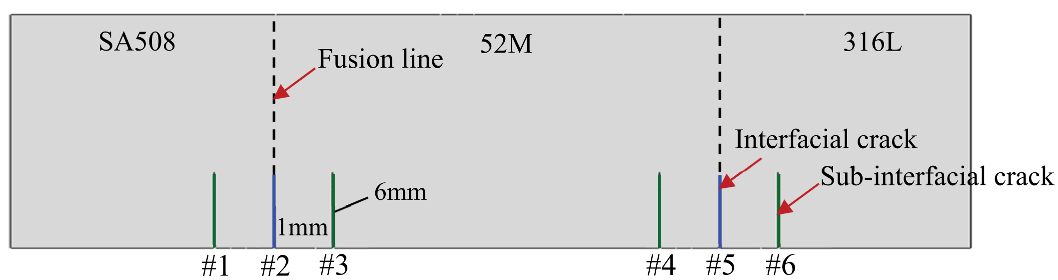

Fig. 8. Schematic diagram of crack locations in a welded joint.

contained 3692 elements, and the secondary submodel consisted of 8738 elements. In Fig. 9, the x-axis is oriented perpendicular to the crack propagation direction, while the positive y-axis aligns with the direction of crack extension. Due to the significant variations in mechanical properties near the weld seam, which induce high stress gradients, the mesh in the vicinity of the crack tip was refined in both the primary and secondary submodels. This refinement ensures a smooth transition and avoids distortion in the crack tip region, thereby facilitating an accurate representation of the mechanical fields [26].

To quantitatively analyze the variation of stress and strain at the crack tip with respect to crack position, observation path 1 was established along the crack propagation direction, while observation paths 2, 3, and 4 were defined as semicircular arcs centered at the crack tip with radii of 1.7 μm, 3 μm, and 4.3 μm, respectively. These paths were used to extract specific parameters of the crack-tip stress and strain fields at different locations. A schematic diagram of the observation paths is shown in Fig. 10. The length of path 1, which captures the crack-tip mechanical fields, is 1.5 μm. Paths 2, 3, and 4 represent semicircular arcs at radial distances of 1.7 μm, 3 μm, and 4.3 μm from the crack tip, respectively.

IV. RESULTS AND DISCUSSIONS

IV.A. Microstructure Results of the DMWJ Interface Area

Fig. 11a through d present the metallographic microstructures of the safe-end DMWJ specimen, showing the SA508 alloy steel (pressure vessel end), the SA508–52Mb interface, the 52Mw–316L interface, and the 316L austenitic SS (piping end), respectively, as revealed by high-magnification microscopy.

Fig. 11a presents the microstructure of the SA508 low-alloy steel, which consists primarily of tempered bainite. Within this structure, regions exhibiting darker and lighter contrasts correspond to areas of higher and lower carbon concentrations, respectively, indicating a nonuniform distribution of carbon within the SA508 alloy.

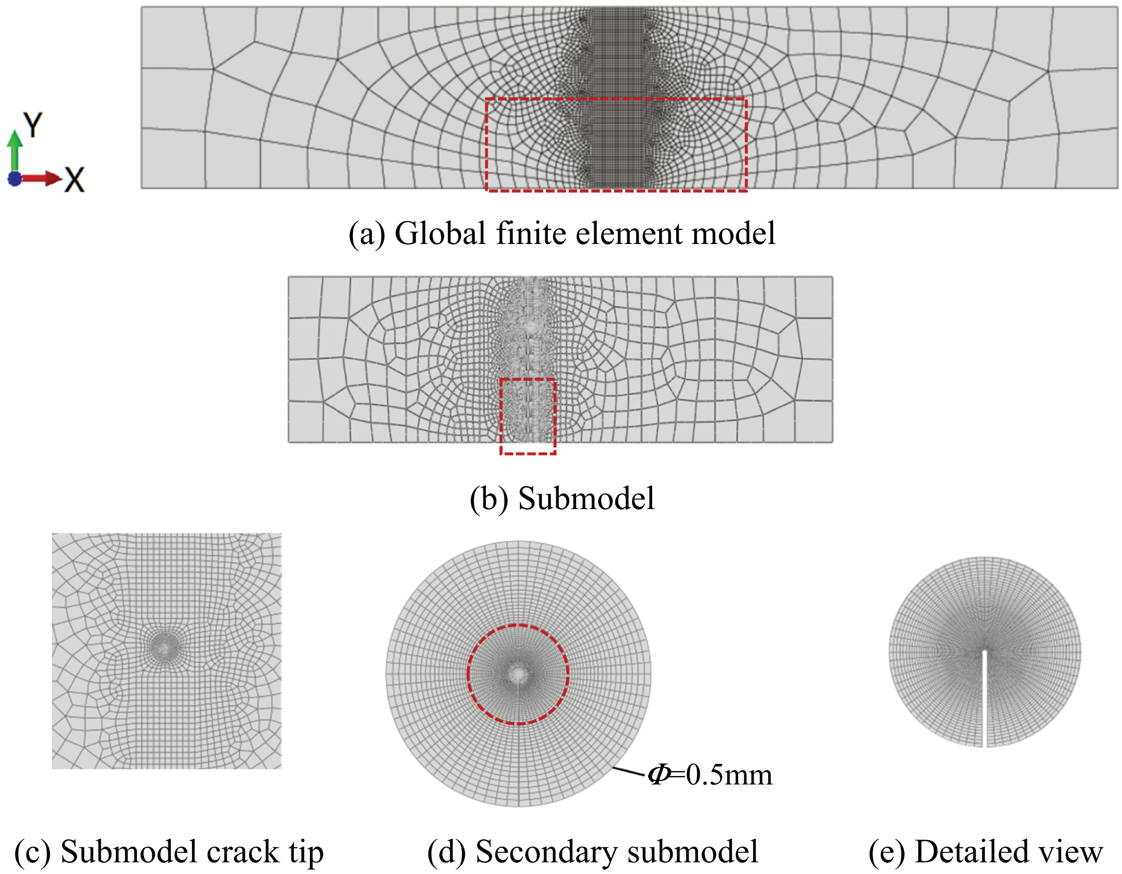

Fig. 9. Finite element mesh model of welded joint with SCC crack.

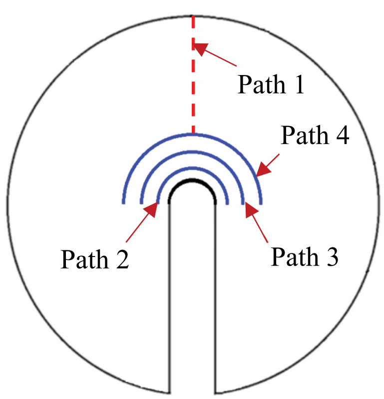

Fig. 10. Schematic diagram of monitoring paths for crack-tip plastic strain field.

Figs. 11b and 11c present the metallographic structures of the SA508–52Mb interface and the 52Mw–316L interface, respectively. Owing to the significant microstructural differences between tempered bainite and austenite, a distinct fusion line is observable in Fig. 11b. Both the buttering layer (nickel-based alloy 52Mb) and the butt WM (alloy 52Mw) exhibit a columnar austenitic structure. However, it is evident that within the buttering layer (52Mb), the grain orientation is predominantly parallel to the welding direction, whereas in the butt weld zone (52Mw), the grains are oriented perpendicular to the weld. According to the literature [27], during the progressive solidification of the weld pool, grains typically grow along the direction of the maximum temperature gradient, which corresponds to the direction of most rapid heat dissipation. Consequently, the difference in the primary heat flow direction resulting from variations in welding procedures is identified as the main reason for the differing grain orientations observed in these structurally similar materials. Fig. 11c reveals the presence of a band-like unmixed zone adjacent to the 52Mw–316L interface. This indicates that the molten nickel-based alloy 52Mw solidified without sufficient mixing with the 316L BM, leading to the formation of this zone. Studies referenced in the literature [2] indicate that the presence of an unmixed zone can create a strength mismatch across the weld, thereby promoting the initiation of SCC.

Fig. 11d presents the metallographic analysis results of the 316L BM located away from the weld zone. The microstructure is characterized as austenitic, with a small number of dark, point-like inclusions observable both

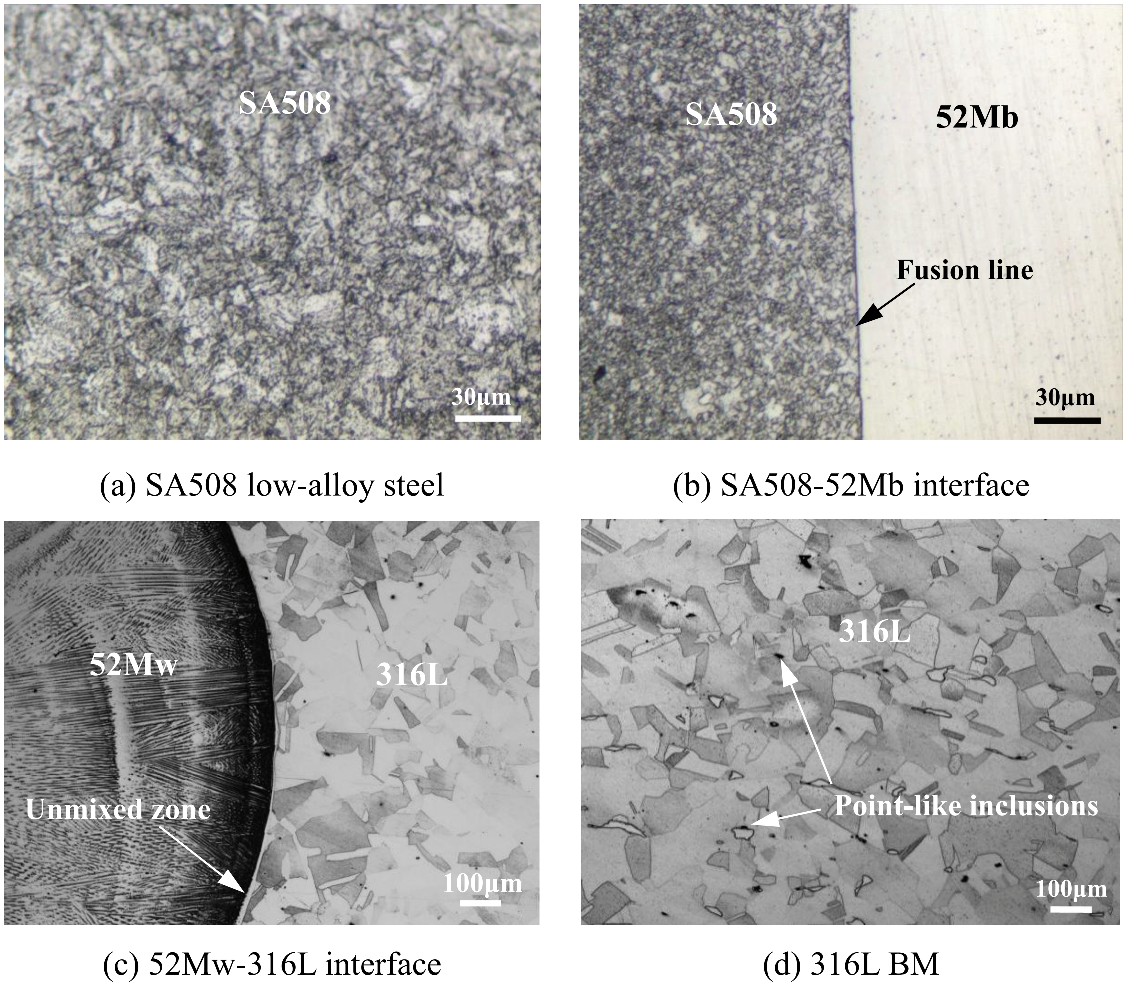

Fig. 11. Microstructure results of the DMWJ interface area.

within the grains and along the grain boundaries. No significant grain growth is evident in the micrograph, indicating that the thermal effects of the welding process had a limited influence on the macroscopic structure of the 316L region distant from the weld.

IV.B. Simulation Results

Mechanistic SCC growth formulations, exemplified by the Ford–Andresen framework [28,29], permit the direct integration of mechanical state variables—specifically crack-tip opening stress and PEEQ. Within these paradigms, crack propagation is governed by the synergistic effects of the crack-tip strain rate (derived from plasticity accumulation) and the local stress state, as quantified by stress triaxiality and opening stress. Consequently, the precise quantification of crack-tip mechanical variables within the DMWJ region is of critical importance. The following analysis focuses on the mechanical state variables at SCC crack tips situated within distinct zones of the DMWJ.

IV.B.1. Effect of Crack Location on the Crack-Tip Stress Distribution in Stress Corrosion Cracks

The Mises stress distributions at the crack tip for cracks at different locations are shown in Figs. 12 through 17. The observation region has a radius of 0.2 mm, and the crack length is uniformly set to 6 mm. In Figs. 12 through 17, cracks #2 and #5 are interface cracks, while cracks #1, #3, #4, and #6 are sub-interface cracks.

Overall, under the condition that the crack location and crack length remain consistent, the Mises stress in the crack tip region computed using the continuous transition model is significantly higher than that obtained with the sandwich model. This indicates that the traditional sandwich model may underestimate the Mises stress at the crack tip when characterizing the crack-tip stress field.

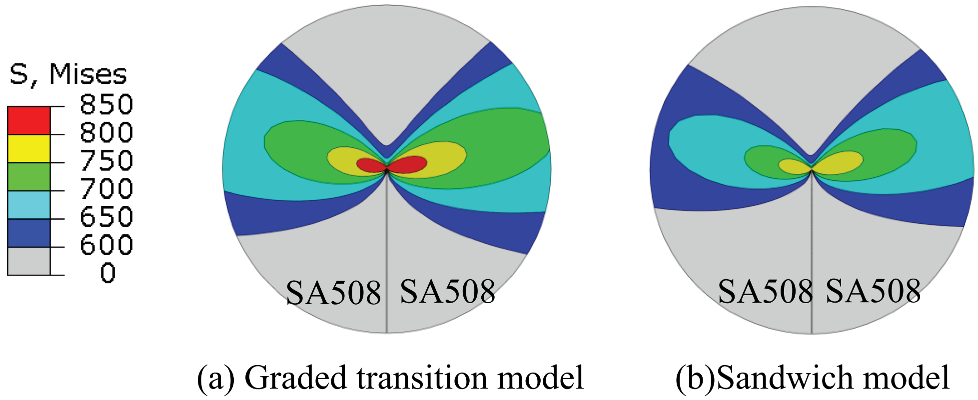

Fig. 12. Mises stress at the tip of sub-interfacial crack #1.

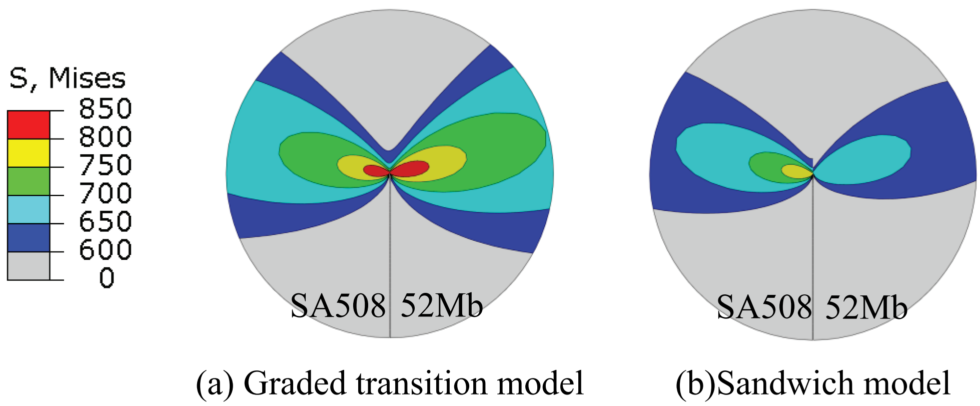

Fig. 13. Mises stress at the tip of interfacial crack #2.

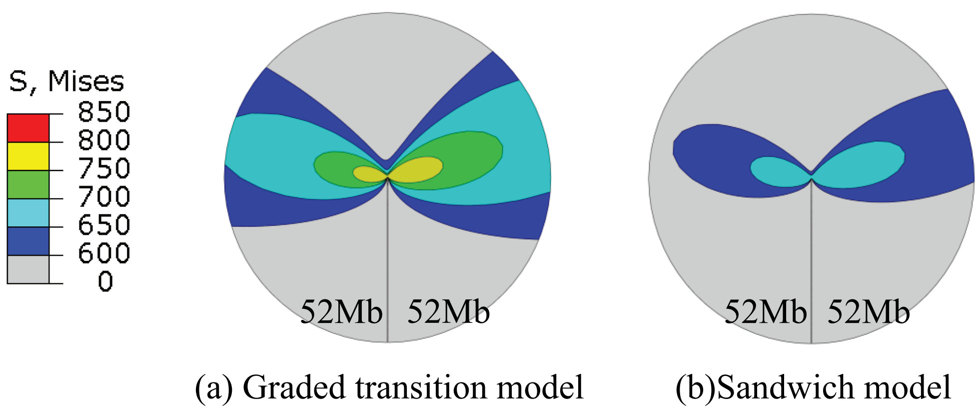

Fig. 14. Mises stress at the tip of sub-interfacial crack #3.

Furthermore, from the stress distribution of interface crack #2 computed with the sandwich model, a distinct discontinuity in the stress distribution can be observed. To quantitatively analyze the stress magnitude at the crack front for different crack locations, the Mises stresses along observation path 1 were extracted at six positions for both the continuous transition model and the sandwich model, as shown in Figs. 18a and 18b. It can be seen that the maximum Mises stress at the crack front is obtained for crack #1 in the heat affected zone of the SA508 BM using the continuous transition model, whereas for the sandwich model, the maximum occurs at crack #2 at the SA508–52Mb interface. Moreover, the Mises stresses at the crack front for all six cracks are higher in the

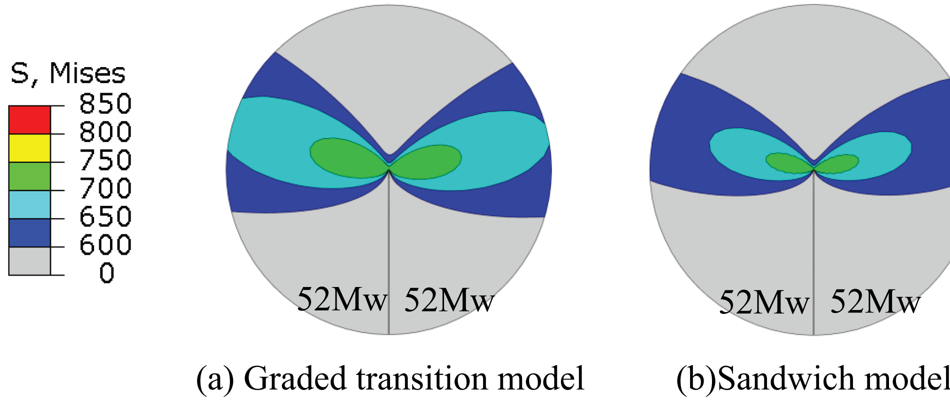

Fig. 15. Mises stress at the tip of sub-interfacial crack #4.

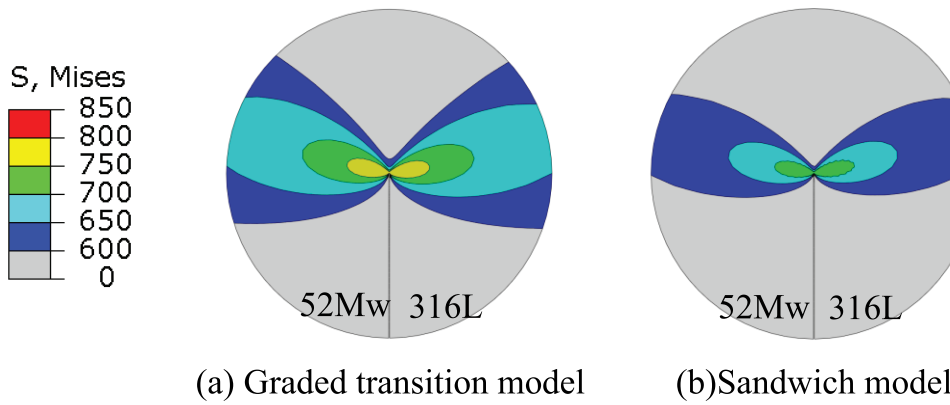

Fig. 16. Mises stress at the tip of interfacial crack #5.

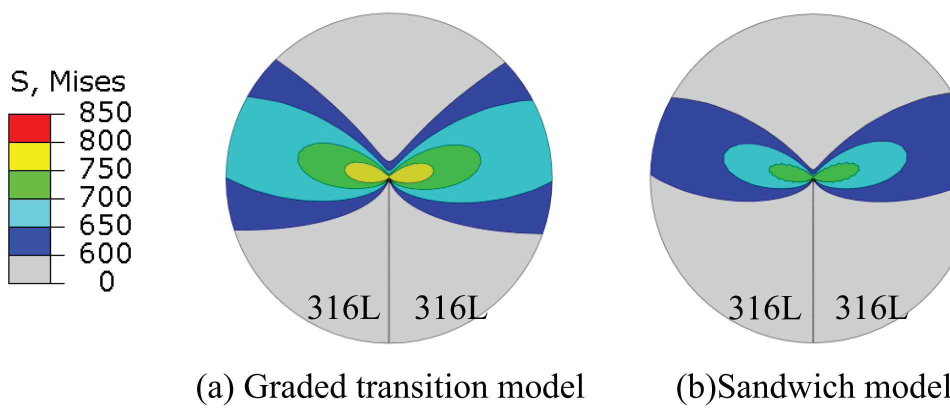

Fig. 17. Mises stress at the tip of sub-interfacial crack #6.

continuous transition model than in the sandwich model, reaffirming that the simplification of material properties in the sandwich model may lead to an underestimation of the Mises stress at the crack front in the weld joint.

The Mises stresses along observation path 2 for the interface cracks at the SA508–52Mb and 52Mw–316L boundaries (crack #2 and crack #5) were extracted from the continuous transition model and the sandwich model, respectively. The results are presented in Figs. 19a and 19b. The Mises stress distribution around the crack tip obtained from the continuous transition model transitions smoothly without any discontinuity. In contrast, the sandwich model exhibits a distinct discontinuity in the Mises stress distribution across the crack tip when characterizing the

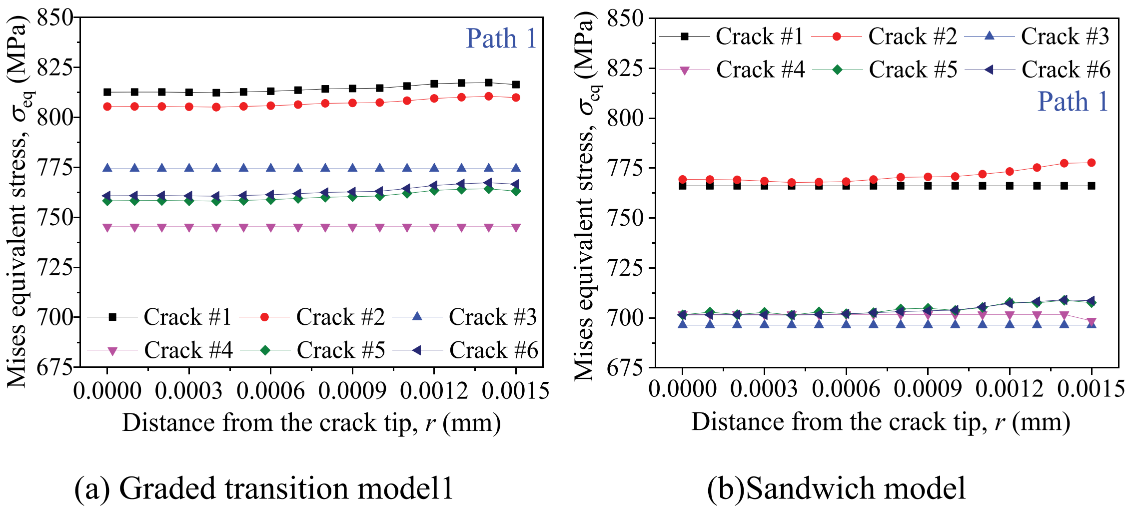

Fig. 18. Comparative analysis of Mises stresses along crack propagation directions for cracks at distinct locations.

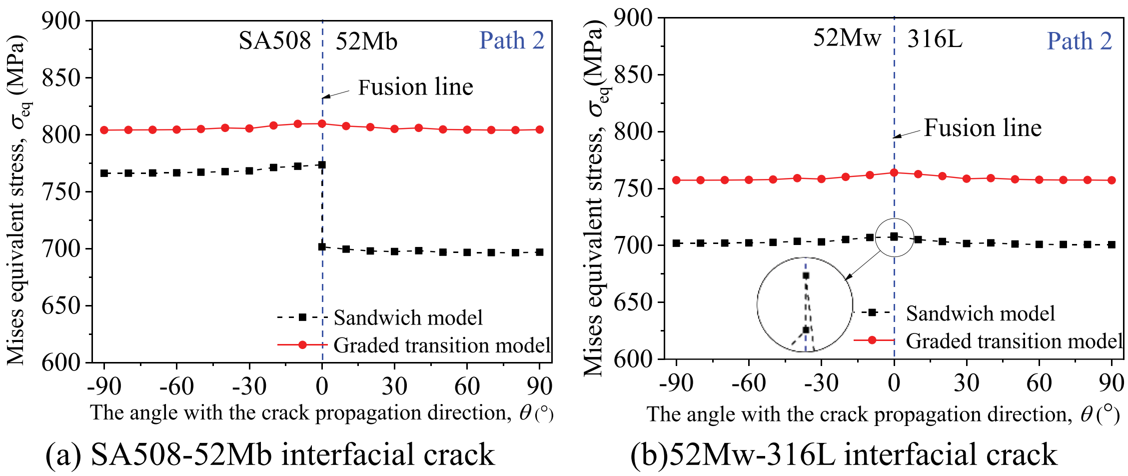

Fig. 19. Comparative analysis of von Mises stress distributions along circumferential directions for interfacial cracks.

SA508–52Mb weld interface crack. On either side of the SA508–52Mb weld, the stress distribution is essentially symmetric in the continuous transition model. However, in the sandwich model, the stress on the SA508 side is significantly higher than that on the 52Mb side, and the Mises stress plummets abruptly at the weld seam. A discontinuity in the calculated stress is also observed at the 52Mw–316L interface when using the sandwich model, although its magnitude is relatively smaller.

A comparison of the computational results from the two models reveals that the Mises stresses at both weld locations obtained using the continuous transition model are consistently higher than those predicted by the sandwich model, which is consistent with the findings presented in Figs. 13 and 16. The distribution of Mises stress on both sides of the crack tip serves as a key indicator for predicting the direction of SCC propagation. The sandwich model, which simplifies the material properties by treating different regions as distinct, introduces an unrealistic discontinuity in the crack-tip stress distribution. This simplification may adversely affect the accurate prediction of SCC crack growth paths in actual welded joints.

IV.B.2. Effect of Crack Location on the Crack-Tip Plastic Strain in Stress Corrosion Cracks

To investigate the variations in plastic strain at crack front regions with different positions, the PEEQ along observation path 1 was calculated using the continuous transition model and the sandwich model for two interface cracks and four near-interface cracks in the fusion line region of SA508–52Mb and 52Mw–316L. The crack length was uniformly set to 6 mm, with the computational results illustrated in Fig. 20.

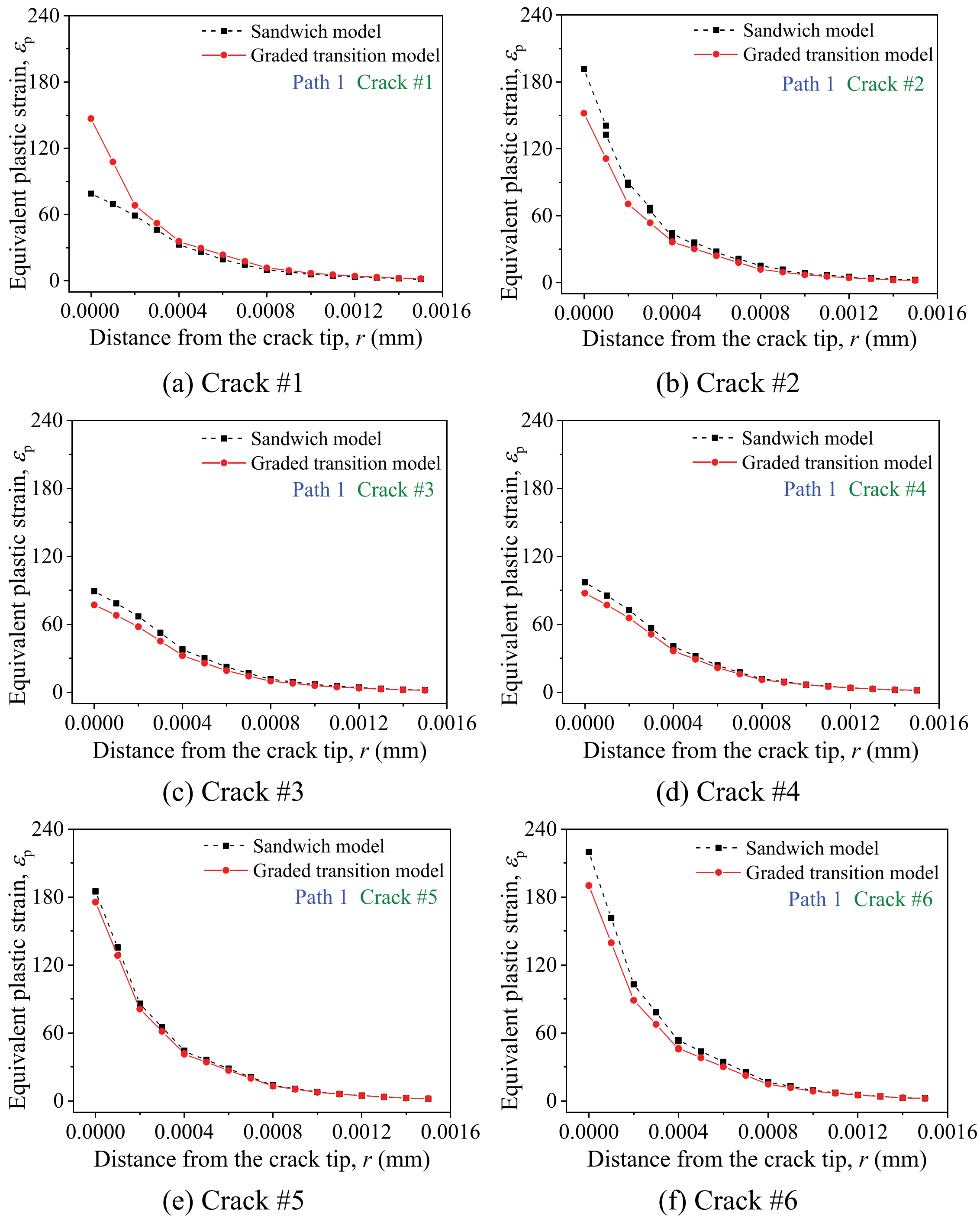

Fig. 20. The variations in PEEQ along observation path 1 at different crack positions.

Results from both the continuous transition model and the sandwich model indicate that crack #6 exhibits the highest PEEQ at the crack tip, while crack #3 shows the lowest. The PEEQ along the crack front gradually decreases as the distance from the crack tip increases. Correspondingly, the difference in PEEQ between the two models along observation path 1 also narrows with increasing distance. With the exception of crack #1, the crack-tip plastic strain computed using the sandwich model is slightly higher than that obtained with the continuous transition model for the other five crack locations. This suggests that, except for cracks located in the HAZ of the SA508 BM on the pressure vessel side, the sandwich model tends to overestimate the magnitude of PEEQ at the crack tip in the remaining regions of this type of welded joint.

The PEEQ along observation paths 2, 3, and 4 for the interface cracks at the SA508–52Mb (crack #2) and 52Mw–316L (crack #5) locations, as computed by both the continuous transition model and the sandwich model, are extracted and shown in Figs. 21 through 23. The results indicate that on either side of the SA508–52Mb weld, the PEEQ on the SA508 side is significantly lower than that on the 52Mb side. Within the 52Mb region, a considerable discrepancy in the PEEQ is observed between the two models, with the sandwich model yielding higher values along all three observation paths. For the 52Mw–316L weld, the distribution of PEEQ is essentially symmetric according to both models, although the sandwich model predicts a slightly higher value on the 316L side compared to the continuous transition model. As the angle between the observation path and the crack propagation direction increases, the PEEQ values on both sides of the weld first increase and then decrease, concurrently, the discrepancy between the results from the two models gradually diminishes. Furthermore, as can be seen from Fig. 21, a "discontinuity" in the PEEQ across the weld is still present in the results obtained with the sandwich model along path 2, though its magnitude is relatively small. Results from Figs. 22 and 23 show that this "discontinuity" in PEEQ predicted by the sandwich model is not pronounced along paths 3 and 4.

When analyzing the SCC crack growth behavior dominated by plastic strain, the use of the sandwich model to compute the plastic strain near the crack tip of a fusion line interface crack in a dissimilar metal welded joint may lead to an overestimation of the plastic strain magnitude on the 52Mb and 316L sides, which could affect the accuracy of predicting the interface crack propagation path in actual welded joints.

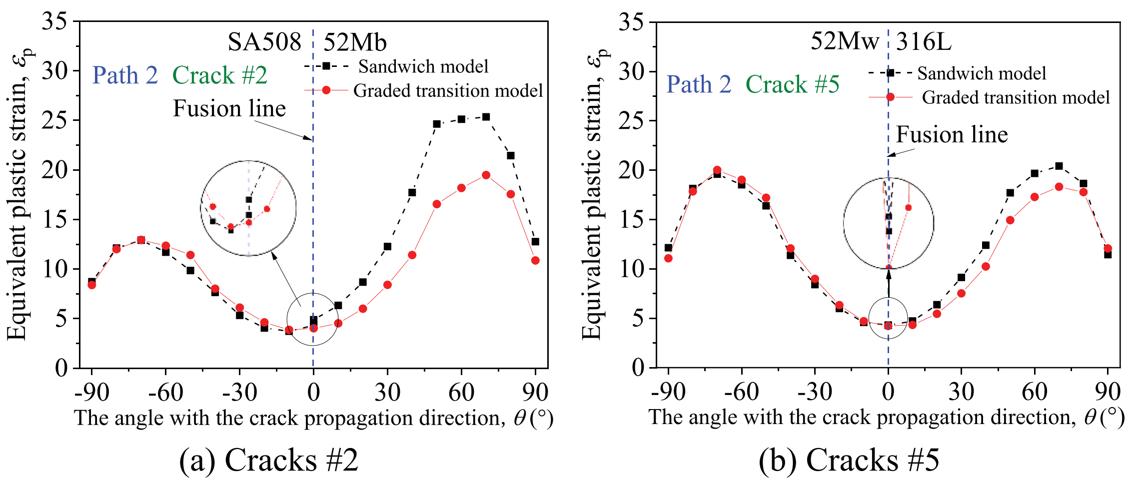

Fig. 21. The PEEQ variations along observation path 2 for different interface cracks.

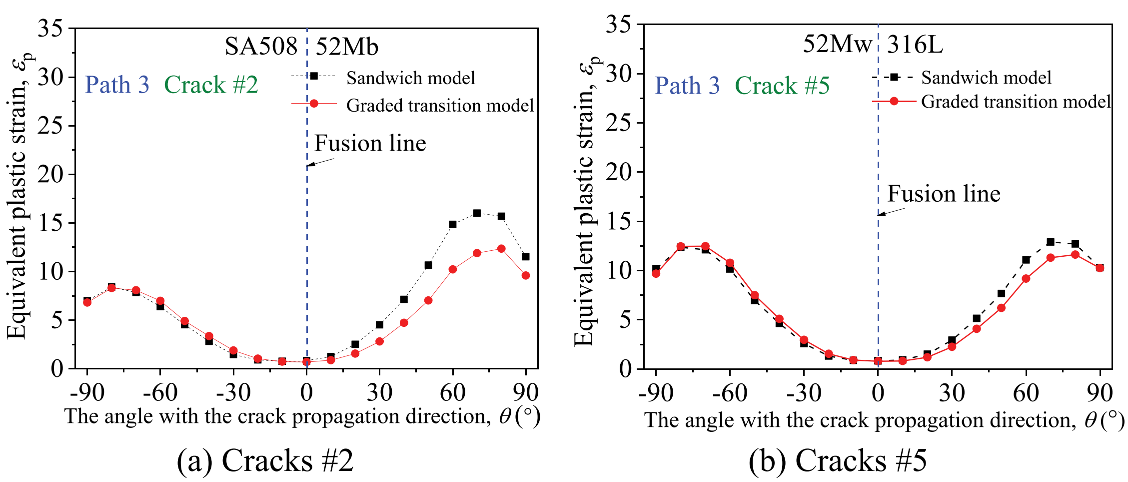

Fig. 22. The PEEQ variations along observation path 3 for different interface cracks.

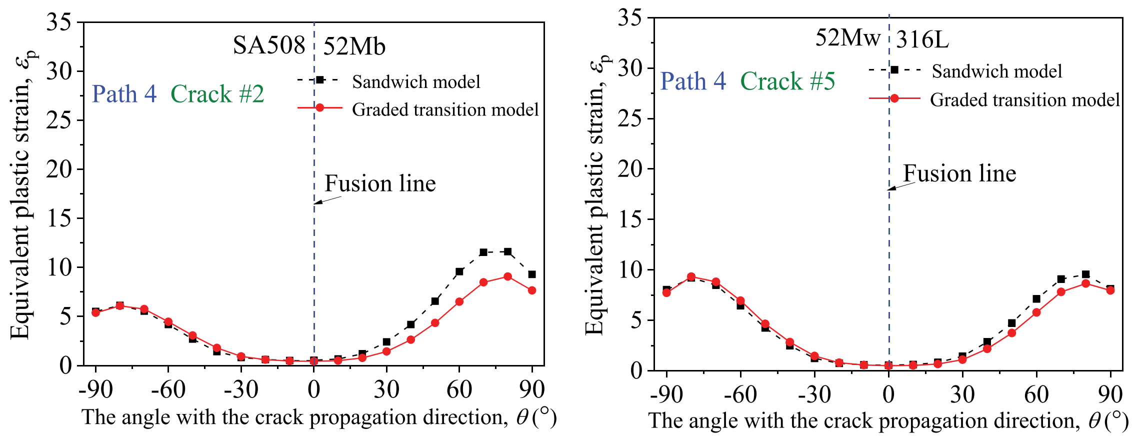

(a) Cracks #2 (b) Cracks #5

Fig. 23. The PEEQ variations along observation path 4 for different interface cracks.

V. CONCLUSIONS

Based on a predefined temperature field methodology, a continuous transition model was developed to precisely capture the mechanical properties of SA508-52M-316L DMWJs. The computational results of Mises stress and PEEQ derived from this continuous model were systematically compared with those obtained from the conventional sandwich model.

Main conclusions are as follows:

1. The SA508 BM exhibits a bainitic microstructure, while the 316L SS consists of an austenitic structure. Both the 52Mb and the 52Mw display a columnar austenitic structure, with grain orientations predominantly parallel and perpendicular to the weld direction, respectively. The presence of an unmixed zone at the 52Mw–316L interface increases the susceptibility of this region to SCC.

2. The utilization of a DMWJ model with continuously transition mechanical properties eliminates the stress and strain discontinuities that arise in traditional sandwich models due to the direct assignment of material properties across the fusion line interface, thereby mitigating the adverse impact of abrupt material property changes on the predictive accuracy of crack growth behavior in DMWJs.

3. Under the condition of consistent crack location and crack length, the Mises stress in the crack-tip region computed using the continuous transition model is significantly higher than that obtained with the sandwich model. Consequently, when employing the sandwich model to calculate the crack-tip stress distribution in DMWJs, the Mises stress at the crack tip may be underestimated.

4. When analyzing the SCC growth of interface cracks dominated by plastic strain, the use of the sandwich model may lead to an overestimation of the PEEQ in both the 52Mb and the 316L HAZ on the pipe side, consequently introducing deviations in the prediction of the interface crack propagation path in DMWJs.

This study aimed to enhance the comprehension of how material inhomogeneity influences the crack growth driving force at the crack tip within DMWJs. While the analysis employed stationary crack tips to evaluate variations in the crack growth driving force during propagation, the current results do not account for the cumulative effects of plastic zone development at the crack tip. The application of dynamic crack propagation methods, such as peridynamics, is anticipated to elucidate these aspects more effectively. Subsequent research will therefore focus on employing these advanced numerical techniques to address this limitation.

Nomenclature

D = Distance from fusion line

E = Young's modulus

F_{max} = Electron backscatter diffraction

h_r = Residual depth

n = Strain hardening exponent

q = Angle with the crack propagation direction

R = Distance from the crack tip

Greek

ε_p = Equivalent plastic strain

σ_{eq} = Mises equivalent stress

σ_y = Yield stress

Acronyms

BM: Base metal

DMWJs: Dissimilar metal weld joints

EBSD: Electron backscatter diffraction

FB: Fusion boundary

FE: Finite element

FL: Fusion line

HAZ: Heat affected zone

NPPs: Nuclear power plants

PEEQ: Equivalent plastic strain

PWR: Pressurized water reactor

SCC: Stress corrosion cracking

SCCGR: Stress corrosion crack growth rate

SENB: Single-edge notched bend

SS: Stainless steel

WM: Weld metal

XFEM: Extended finite element method

Author Contributions

CRediT: **Shuai Wang:** Data curation, Formal analysis, Software, Visualization, Writing – original draft; **Yicheng Wang:** Visualization, Writing – original draft; **Bin Wang:** Funding acquisition, Project administration, Resources, Writing – review & editing; **Wanzhong Li:** Resources, Writing – review & editing; **Lu Cui:** Project administration, Resources, Visualization; **Shaohu Liu:** Project administration, Resources; **Lijing Dong:** Data curation, Formal analysis, Visualization; **He Xue:** Conceptualization, Funding acquisition, Supervision, Writing – review & editing.

Disclosure Statement

No potential conflict of interest was reported by the author(s).

Funding

This work was financially supported by Natural Science Basic Research Plan in Shaanxi Province, China [2026JC-YBMS-0538]; Royal Society, UK [IEC\NSFC\233524]; State Key Laboratory of Petroleum Resources and Engineering, China University of Petroleum (Beijing) [No.PRE/open-2606]; Scientific Research Program Funded by Shaanxi Provincial Education Department [25JP143]; Qin Chuang Yuan "Scientist and Engineer" Team Construction of Shaanxi Province of China [2025QCY-KXJ-026].

ORCID

Shuai Wang http://orcid.org/0000-0002-5601-0385
Bin Wang http://orcid.org/0000-0002-1398-6599
Lijing Dong http://orcid.org/0000-0002-8484-7537
He Xue http://orcid.org/0000-0002-4525-0404

References

1. H. Ming et al., "Microstructure of a Safe-End Dissimilar Metal Weld Joint (SA508-52-316L) Prepared by Narrow-Gap GTAW," *Mater. Charact.*, **123**, 233 (2017); https://doi.org/10.1016/j.matchar.2016.11.029.
2. L. Dong et al., "Microstructure and Intergranular Stress Corrosion Cracking Susceptibility of a SA508-52M-316L Dissimilar Metal Weld Joint in Primary Water," *J. Mater. Sci. Technol.*, **34**, *8*, 1281 (2018); https://doi.org/10.1016/J.JMST.2017.11.051.
3. Q. Wang et al., "Study of Type-II Boundary Behavior During SA508-3/EQ309L Overlay Weld Interfacial Failure Process," *J. Mater. Process. Technol.*, **247**, 64 (2017); https://doi.org/10.1016/j.jmatprotec.2017.04.009.
4. S. Wang et al., "Effects of Angles and Shapes of a Corner Crack on the Driving Force at a Set-In Nozzle-Cylinder in a PWR Pressure Vessel," *Ann. Nucl. Energy*, **192**, 109991 (2023); https://doi.org/10.1016/j.anucene.2023.109991.
5. L. Dong et al., "Effect of Surface Treatments on Microstructure and Stress Corrosion Cracking Behavior of 308L Weld Metal in a Primary Pressurized Water Reactor Environment," *Corros. Sci.*, **166**, 108465 (2020); https://doi.org/10.1016/j.corsci.2020.108465.
6. U. Ehrnstén, P. L. Andresen, and Z. Que, "A Review of Stress Corrosion Cracking of Austenitic Stainless Steels in PWR Primary Water," *J. Nucl. Mater.*, **588**, 154815 (2024); https://doi.org/10.1016/j.jnucmat.2023.154815.
7. L. Dong et al., "Microstructure and Stress Corrosion Cracking of a SA508-309L/308L-316L Dissimilar Metal Weld Joint in Primary Pressurized Water Reactor Environment," *J. Mater. Sci. Technol.*, **40**, 1 (2020); https://doi.org/10.1016/j.jmst.2019.08.035.

8. G. X. Chen et al., "Effect of Strength Mismatch on Limit Load of Dissimilar Metal Welded Joint for Connecting Pipe-Nozzle of Nuclear Pressure Vessel," *Eng. Fract. Mech.*, **272**, 108699 (2022); https://doi.org/10.1016/j.engfracmech.2022.108699.
9. W. Sun et al., "Stress Corrosion Cracking Behavior at Fusion Lineof Cold Worked 316LN Stainless Steel/ Inconel 52 M Weld Joint in Simulated Primary Water Environment," *Corros. Sci.*, **242**, 112581 (2025); https://doi.org/10.1016/j.corsci.2024.112581.
10. B. O. Okonkwo et al., "Microstructural Characterization of Low Alloy Steel A508–309/308L Stainless Steel Dissimilar Weld Metals," *Int. J. Press. Vessels Pip.*, **190**, 104297 (2021); https://doi.org/10.1016/j.ijpvp.2020.104297.
11. B. O. Okonkwo et al., "A New Method to Determine the Synergistic Effects of Area Ratio and Microstructure on the Galvanic Corrosion of LAS A508/309 L/308 L SS Dissimilar Metals Weld," *J. Mater. Sci. Technol.*, **78**, 38 (2021); https://doi.org/10.1016/j.jmst.2020.10.044.
12. Z. Wang et al., "A Multi-Method Coupled Approach to Simulate Crack Growth Path and Stress-Strain Field at the Tip of the Growing Crack in the Dissimilar Metal Welded Joint," *Int. J. Press. Vessels Pip.*, **206**, 105046 (2023); https://doi.org/10.1016/j.ijpvp.2023.105046.
13. L. Zhao, B. Yang, and Y. Sun, "Crack-Tip Constraint Analysis of the Dissimilar Metal-Welded Joint and Constraint Match with Test Specimens," *Nucl. Sci. Eng.*, **199**, *9*, 1512 (2025); https://doi.org/10.1080/00295639.2025.2456369.
14. J. Yang and L. Wang, "Effect and Optimal Design of the Material Constraint in the DMWJ of Nuclear Power Plants," *Acta Metall. Sin.*, **56**, *6*, 840 (2020); https://doi.org/10.11900/0412.1961.2019.00298.
15. S. Wang et al., "Investigation of the Inhomogeneous Mechanical and Crack Driving Force of Low Alloy Steel SA508 and Its Welded 309L/308L Stainless Steel Cladding," *Nucl. Sci. Eng.*, **197**, 623 (2022); https://doi.org/10.1080/00295639.2022.2123210.
16. S. Zhang et al., "Effect of Mechanical Heterogeneity on Strain and Stress Fields at Crack Tips of SCC in Dissimilar Metal Welded Joints," *Materials*, **14**, *16*, 4450 (2021); https://doi.org/10.3390/ma14164450.
17. S. Gu et al., "Effect of Residual Stress Introduced by Local Loading on Fracture Behaviour of DMWJ Under Different Constraints," *Int. J. Press. Vessels Pip.*, **202**, 104885 (2023); https://doi.org/10.1016/j.ijpvp.2023.104885.
18. H. T. Wang et al., "An Experimental Investigation of Local Fracture Resistance and Crack Growth Paths in a Dissimilar Metal Welded Joint," *Mater. Des.*, **44**, 179 (2013); https://doi.org/10.1016/j.matdes.2012.07.067.
19. H. T. Wang et al., "Fracture Mechanism of a Dissimilar Metal Welded Joint in Nuclear Power Plant," *Eng. Fail. Anal.*, **28**, 134 (2013); https://doi.org/10.1016/j.engfailanal.2012.10.005.
20. GB/T 22458-2008, "General Rules of Instrumented Nanoindentation Test," Standardization Administration of China, China Quality and Standards Publishing and Media Company Limited (2012). https://openstd.samr.gov.cn/bzgk/gb/newGbInfo?hcno=D41A27970B0503F50A414F4D519B0DD0.
21. S. Wang, "Study on the Effect of Material Inhomogeneity on Mechanical State at Crack Tip of the Safety End Welded Joint in Nuclear Power Plant," Doctoral Dissertation, Xi'an University of Science and Technology (2021). https://doi.org/10.27397/d.cnki.gxaku.2021.001052.
22. S. Wang et al., "Study on the Mechanical State of Inner Surface Crack Tips at SA508-52M-316L Dissimilar Metal Welded Joint Interfaces," *Eng. Fract. Mech.*, **339**, 112126 (2026); https://doi.org/10.1016/j.engfracmech.2026.112126.
23. K. Fan, "Study on Local Fracture Behavior of Materials Interface Regions in Dissimilar Metal Welded Joints in Nuclear Power Plant," Doctoral Dissertation, East China University of Science and Technology (2018).
24. M. De Beule et al., "Plasticity as a Lifesaver in the Design of Cardiovascular Stents," *Key Eng. Mater.*, **340**, 841 (2007); https://doi.org/10.4028/www.scientific.net/KEM.340-341.841.
25. H. T. Wang et al., "Local Mechanical Properties of a Dissimilar Metal Welded Joint in Nuclear Power Systems," *Mater. Sci. Eng.*, **568**, 108 (2013); https://doi.org/10.1016/j.msea.2013.01.037.
26. S. Wang et al., "Effects of the Surface Crack Shape on J Values Along the Front of an Elliptical Crack," *Fatigue Fract. Eng. Mat. Struct.*, **44**, *11*, 2944 (2021); https://doi.org/10.1111/ffe.13522.
27. H. L. Ming et al., "Microstructure and Local Properties of a Domestic Safe-End Dissimilar Metal Weld Joint by Using Hot-Wire GTAW," *Acta Metall. Sin.*, **53**, *1*, 57 (2017); https://doi.org/10.11900/0412.1961.2016.00135.
28. F. P. Ford and P. L. Andresen, "Development and Use of a Predictive Model of Crack Propagation in 304/316L, A533B/A508, and Inconel 600/182 Alloys in 2880°C water[C]," G. J. Theus and J. R. Weeks, Eds., *Proc. 3rd Int. Symp. on Environmental Degradation of Mats. In Nucl. Power Systems-Water Reactors*, Warrendale, Pennsylvania, p. 789, TMS (1988).
29. F. P. Ford, "Quantitative Prediction of Environmentally Assisted Cracking," *Corros. J. Sci. Eng.*, **52**, *5*, 375 (1996); https://doi.org/10.5006/1.3292125.